ELSEVIER

Contents lists available at ScienceDirect

# Acta Materialia

journal homepage: www.elsevier.com/locate/actamat



Full length article

# On the plastic deformation of a CoCrFeNiW-C alloy at elevated temperatures: Part I. Serrated plastic flow and its latent dynamics



Shaolou Wei, Daniel P. Moriarty, Michael Xu, James M. LeBeau, Cemal Cem Tasan\*

Department of Materials Science and Engineering, Massachusetts Institute of Technology, Cambridge MA02139, USA

#### ARTICLE INFO

Article history:
Received 11 June 2021
Revised 8 October 2022
Accepted 11 October 2022
Available online 14 October 2022

Keywords: Chaotic dynamics Slip intermittency Thermal activation Superalloys

#### ABSTRACT

Multi-component Co-alloys are a class of promising metallic materials for high-temperature applications. The present work primarily focuses on the plastic deformation mechanisms of a CoCrFeNiW-C alloy at 650 °C, with emphases on dislocation slip intermittency and plastic flow features. To this end, by integrating *in situ* scanning electron microscopy-based tests, statistical analyses, and theoretical calculations, several mechanistic insights are revealed. In this material, the plastic flow is featured by evident serration events with a self-organized critical dynamic feature, where mixed Type A and B serrations operate at a moderate deformation level, followed by the onset of a higher magnitude Type B serration. As temperature increases up to 700 and 750 °C, although more evident Type C serration occurs, the self-organized criticality along with the spatial-temporal power-law scaling relation remains nearly unaffected. Microstructural relevance of the serration mechanisms and the deformation substructural characteristics are also explored in greater depth.

© 2022 Acta Materialia Inc. Published by Elsevier Ltd. All rights reserved.

#### 1. Introduction

The growing demands in seeking structural materials that can endure higher temperatures and more aggressive service environments have led to a robust momentum in advancing metallic alloy design [1–3]. Beyond Ni-based superalloys, ordered  $\gamma$ -TiAl alloys, and the emerging concentrated refractory alloys, multi-component Co alloys are also considered as promising materials for extreme environments. Co, with its high melting temperature, the capability to form solid solution microstructures with a variety of transition elements (e.g. Cr, Fe, Ni, and Mo) [4,5], and the potential to develop beneficial precipitates (e.g. the Co<sub>3</sub>(Al, W) L1<sub>2</sub> phase [6–8]) enables an immense alloy design space. Recent literature [9,10] also reflects the trend of introducing transition metal carbides and/or nitrides to enhance the softening resistance of these alloys.

From a mechanics standpoint, load-bearing performance and the underlying plastic deformation micro-mechanisms of multicomponent Co-alloys also reveal great complexity and have drawn significant attention. Because of the relatively low intrinsic stacking fault energy ( $\gamma_{\rm ISFE}$ ), operative plastic deformation modes in Co-alloys reveal some similarities with other face-centered cubic (FCC) structured ferrous alloys at room temperature. Depending on the magnitude of  $\gamma_{\rm ISFE}$ , perfect dislocation slip [11], mechanical twinning [12], strain-induced martensitic transformation [13], and most

\* Corresponding author.

E-mail address: tasan@mit.edu (C.C. Tasan).

recently, mechanical faulting [14] have all been documented in Coalloys, and consequently, leading to various strength-ductility combinations. On the other hand, elevated temperature effects have been explored in the literature in two directions, focusing on: (1) the time-dependent plastic flow response under stress (i.e. creep) [6]; and (2) the temperature-dependent yield strength preservation [10,15]. The present research is motivated instead to explore the quasi-static elevated temperature plastic flow characteristics in these materials, as well as the underlying deformation micromechanisms that lead to them.

Phenomenologically, one of the most challenging complexities of plastic deformation at elevated temperatures lies in the presence of serrated flow, a type of plastic response featured by consecutive discernable stress drops (or strain jumps) in the stress-strain curves [16]. The historical viewpoint of this phenomenon can be traced back to Cottrell and Bilby [17] who conceived that mobilized carbon interstitial clouds were responsible for the serrated yielding behavior in iron. The investigation of the microstructural origins for serration is common in light metals (i.e. Al- or Mgalloys) and steels, but less so in Co- or Ni-based high-temperature alloys. In the few records that have reported detailed mechanistic investigations [18-22], the following characteristics are generally recognized for Co- and Ni-based alloys: (1) under a quasi-static (strain rate  $\dot{\varepsilon}=10^{-3}~\text{s}^{-1}$ ) uniaxial tensile loading condition, serrated plastic flow takes place roughly in the temperature range of 400-700 °C; (2) keeping the same quasi-static strain rate, the elevation of testing temperature leads to a transition of dominant

serration mode from Type A to Type B and eventually Type C (a more detailed discussion of these serration modes is provided in Section 3.2); and (3) the presence of the ordered L1<sub>2</sub> phase has been hypothesized to act as a sink for interstitial solute while enabling a strong pinning effect for mobile dislocations. Besides the complex microstructural mechanisms for serrated plastic flow, the noise-like features of these small avalanche incidents have also led to growing interest in theoretical modeling and simulation. Typically, two topics are of central interest for assessment: first, what are the statistical attributes of the serration magnitude (i.e. stress drops or strain jumps) and its duration? Second, are the serration magnitude and duration inter-correlated? In response to these, discrete dislocation dynamics models [23,24], finite element methods [25,26], and phase-field crystal models [27] have been so far developed to uncover the statistical regularity embedded in the seemingly chaotic serration incidents.

From a microstructural standpoint, resolving plastic deformation mechanisms and their correlation with damage modes at elevated temperatures can be challenging. Post-mortem characterization, for example, may not always reveal the full nature of microstructural evolution, plasticity, and damage micro-events prior to fracture [28,29]. Even in alloys with a single FCC phase constituent, depending on the local plasticity micro-mechanisms, the plastic strain distribution can be significantly heterogeneous [30,31], causing complex damage mechanisms. Recent advancements in scanning electron microscopy (SEM)-based in situ hightemperature techniques [32] provide opportunities to address these challenges in correlating plasticity and damage mechanisms. With a millimeter level field of view and a nanometer scale of spatial resolution, this kind of technique has demonstrated great potential in achieving synchronous characterization of plastic deformation micro-mechanisms and microstructural evolution [29,33]. A recent report [34] also reveals the capability of in situ SEM-based testing methods to couple with theoretical calculation and crystal plasticity simulation in elucidating the grain boundary properties of Ni-based superalloys.

In this report, we systematically study the plastic deformation mechanisms of a CoCrFeNiW-C alloy at 650 °C via integrated in situ characterization, statistical analyses, and theoretical calculations. It is recognized that, in comparison to the smooth stress-strain response at ambient temperature, the CoCrFeNiW-C alloy exhibits an evident serrated plastic flow at 650 °C under uniaxial tensile loading with a strain rate of  $10^{-3}$  s<sup>-1</sup>. By statistically assessing the serration magnitude and duration, we show that the serration response of this alloy develops a self-organized critical dynamic feature, in which the power-law scaling relation is confirmed for serration magnitude, serration duration, as well as the magnitudeduration correlation. Coupled mechanical measurements and finescale electron microscopy study show that the higher magnitude Type B serration is largely related to L12-type short range ordered domains. When keeping the same  $10^{-3}$  s<sup>-1</sup> strain rate but increasing the testing temperatures up to 700 and 750  $^{\circ}\text{C}$ , although Type C serration becomes more predominant, the underlying selforganized criticality and the power-law scaling properties are still preserved.

# 2. Material and methods

# 2.1. Microstructural characterization and mechanical testing at ambient temperature

The alloy employed in the present study is a fully-recrystallized multi-component Co-based alloy with a nominal composition Co-22.6Cr-1.8Fe-22.9Ni-14.5W-0.11C wt%  $(Co_{40.61}Cr_{27.31}Fe_{2.03}Ni_{24.52}W_{4.96}C_{0.58}, at%)$ , supplied by Allegheny Technologies Incorporated (ATI), Natrona Heights, PA, U.S.A. (non-

commercial grade). Microstructural analyses of this alloy, including secondary and backscattered electron imaging (SE and BSE), electron backscatter diffraction (EBSD), and energy dispersive X-ray spectroscopy (EDS), electron channeling contrast imaging (ECCI) were all carried out in a TESCAN MIRA 3 SEM. The raw Kikuchi diffractograms in EBSD measurement were post-processed in an Orientation Imaging Microscopy (OIM) software (Version 8.0) and an open-access MTEX Toolbox to acquire quantitative information for crystallographic computations. To quantitatively assess the deformation substructure, a home-built open-access STrCryst software [35] was employed to aid the ECCI characterization. Crystallographic orientation information (i.e. the Euler angles) obtained from the EBSD measurement was utilized to identify the activated slip system and to calculate the Schmid factor. Considering the FCC symmetry of the present alloy, our theoretical calculations have presumed a stringent validity of the Schmid's law (i.e. negligible non-glide stress effect), specifically: (1) only the  $\{111\}\langle 1\bar{1}0\rangle$  slip system can be activated; and (2) the identified slip trace signifies the slip direction with the highest Schmid factor among all three possible variants. All of the microstructural specimens were prepared following the standard metallographic routes: mechanical grinding on a series of SiC abrasive papers (400-800 grit), polished with diamond suspension (particle sizes: 9, 3, and 1  $\mu$ m), and finally polished using ~40 nm colloidal SiO<sub>2</sub> for  $\sim$ 30 min.

Phase constitution was investigated with high-energy synchrotron X-ray diffractometry (SXRD) at Beamline 11ID-C, Argonne National Laboratory, Chicago, U.S.A. Two-dimensional diffractograms were collected under a high-energy X-ray beam with 0.1173 Å wavelength, 0.5 mm beam size, and 10 s exposure time at a working distance of 1517.86 mm (calibrated by the NIST-standard CeO<sub>2</sub> powder). To unambiguously assess the diffraction information, the two-dimensional diffractograms were subjected to 5.0° azimuthal integration (87.5-92.5°) along the loading direction (parallel to the rolling direction, RD), and Rietveld refined in a GSAS-II open-access software [36] down to  $R_{wp}$  < 8.0 %. Note that for the specimen fractured at elevated temperature, SXRD patterns were taken right at the fracture end, at which the local plastic strain level is presumably the highest. High-angle annular dark-field (HAADF) scanning transmission electron microscopy (STEM) images were acquired with a Thermo Fisher Scientific Themis Z probe aberration-corrected STEM. A Revolving STEM (RevSTEM) method [37] was utilized for drift correction during imaging. In order to avoid any potential artifact caused by electro-chemical thinning in a multiphase alloy, the TEM specimens were first mechanically ground down to  $\sim$ 20  $\mu$ m thickness under acetone lubrication, then subjected to ion-milling to achieve final perforation. For mechanical property assessment at room-temperature (25 °C), rectangular dog bone-shaped specimens with 6.5 mm  $\times$  2.5 mm  $\times$  1.0 mm gauge dimension for the uniaxial tensile test were sectioned by electrical discharge machining (EDM). Surfaces of these specimens were speckle-patterned for digital image correlation analysis. When being tested on a Diben Gatan micro-mechanical testing instrument (quasi-static condition, strain rate  $\dot{\varepsilon} = 10^{-3} \text{ s}^{-1}$ ), optical images were taken every 1 s and were analyzed in a commercial GOM Correlate software to compute plastic strain. At least three specimens were tested to ensure repeatability of the results.

# 2.2. In situ mechanical testing at elevated temperature

Plastic deformation mechanisms of the present alloy were primarily investigated in an *in situ* manner at an elevated temperature of 650 °C. Fig. 1 details the *in situ* high-temperature deformation setup. A Kammrath & Weiss tensile testing stage equipped with a contact heating module was installed in the chamber of the TESCAN MIRA 3 SEM (Fig. 1(a)). A high-temperature BSE

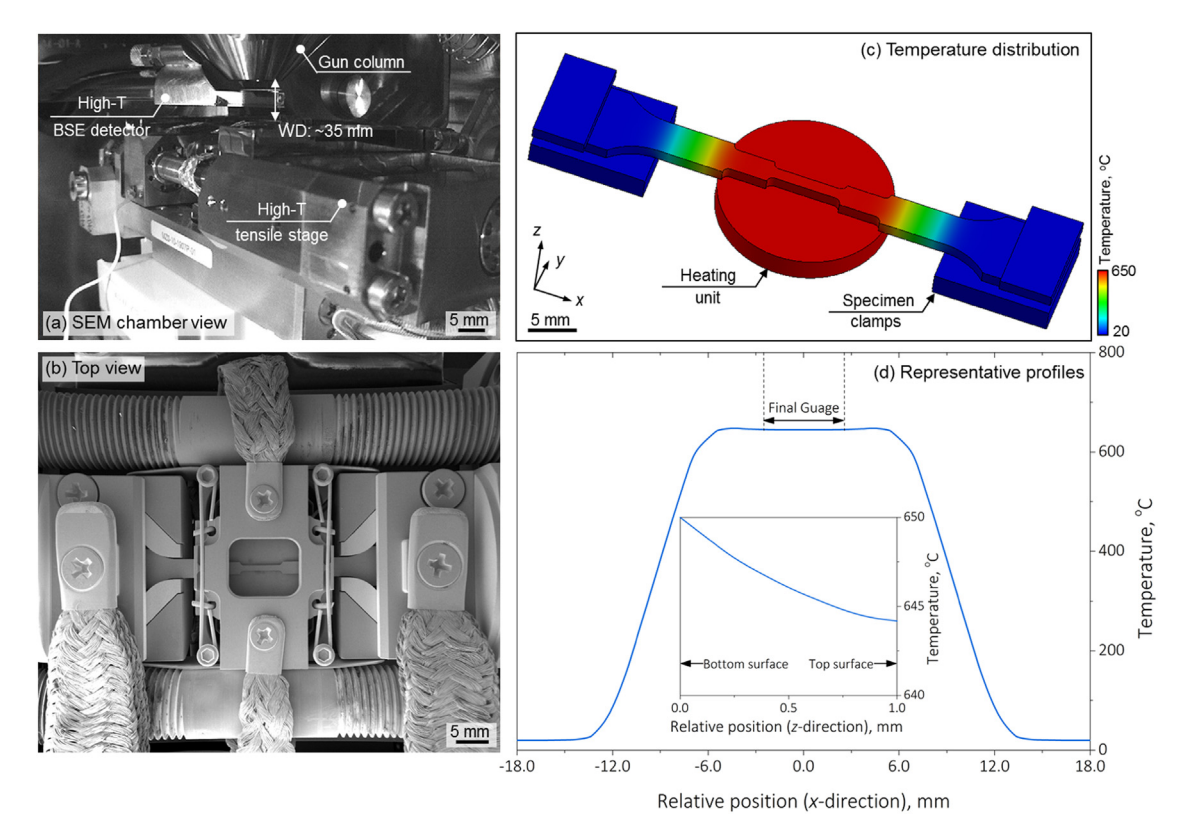


**Fig. 1.** *In situ* experimental setup: (a) SEM chamber view; (b) low-magnification SE-micrograph top view of the testing stage; (c) simulation results of the equilibrium temperature distribution; (d) one-dimensional temperature profile acquired at the central line of the specimen. Inset in (d) shows the temperature difference between bottom and top surfaces.

detector was adopted to acquire microstructural imaging during plastic deformation (working distance  $\sim$ 35 mm). For reliable micro-mechanical deformation study at elevated temperatures, specimen design and assessment of temperature distribution are important. Examining the configuration of the setup (Fig. 1(b)) together with the heat transfer boundary conditions, we have carried out a finite element simulation of the temperature field, of which the computational details are summarized in Appendix A. The final-optimized tensile specimen exhibits gauge dimensions of 5.0 mm  $\times$  1.0 mm  $\times$  1.0 mm, and its more detailed dimensions are provided in Supplementary Fig. S1. Fig. 1(c) presents the simulated equilibrium temperature distribution at a heating unit (considered as a heat reservoir, see Appendix A) temperature of 650 °C. The one-dimensional profile (Fig. 1(d)) taken at the central line along the x-direction confirms the uniform temperature distribution across the gauge section. The inset of Fig. 1(d) validates that the temperature difference between the top and the bottom surfaces is less than ~6 °C through the 1 mm thickness. Unless pronounced necking takes place, which may cause significant contraction in the z-direction, the current sample geometry design ensures a reasonably homogenous temperature distribution during the in situ experiment.

The present high-temperature deformation study was also carried out under a quasi-static loading condition (strain rate  $\dot{\varepsilon} = 10^{-3} \text{ s}^{-1}$ ). In both monotonic (i.e. specimen directly deformed to failure) and interrupted (i.e. deformation with imaging intervals) in situ tests, the specimen was first heated up to the targeted temperature with 50 °C/min heating speed, then equilibrated for 10 min before loading. To quantify the dynamic stress features during high-temperature deformation, datum points were acquired every 0.015 s. Because the stress measurement precision of the current equipment is  $\sim$ 0.1 MPa, to rigorously ensure the validity of

the serration analyses, we have chosen 0.5 MPa as a threshold to distinguish serration and random noise. It should also be noted that due to the absence of an extensometer in these elevated temperature measurements, the engineering strain value was derived using the machine's displacement gauge. Thus the elongation data in the present study cannot be utilized to accurately interpret the loading-bearing performance of the alloy.

#### 3. Results

### 3.1. Undeformed microstructure

The undeformed CoCrFeNiW-C alloy exhibits a near-equiaxed grain morphology (averaged grain size  $\sim\!20.61~\mu m$ , excluding  $\Sigma 3$  twin boundaries, see Supplementary Fig. S2) with an FCC phase as matrix with embedded  $M_{23}C_6$ -type carbide phase (Fig. 2(a), (c1) and (c2)). Fig. 2(b) reveals the {001}, {011}, and {111} pole figures of the matrix FCC phase, in which a weak fiber texture can be seen from the {011} pole figure. Lattice constant of the FCC phase is determined as  $a=3.586~{\rm \mathring{A}}$  through Rietveld refinement of the SXRD patterns. An EDS line profile taken along the  $M_{23}C_6$  phase suggests a prominent enrichment in W but depletion in Co, Cr, and Ni. The  $M_{23}C_6$  phase in the present alloy has a spatially uniform distribution with no preferential presence along grain or twin boundaries.

#### 3.2. Stress-strain response and serration behavior

Fig. 3(a) compares the uniaxial tensile response for the investigated CoCrFeNiW-C alloy at ambient and elevated temperatures. At 25 °C, this alloy yields at  $\sim$ 427.2 MPa, followed by a pronounced strain hardening, reaching an ultimate tensile strength

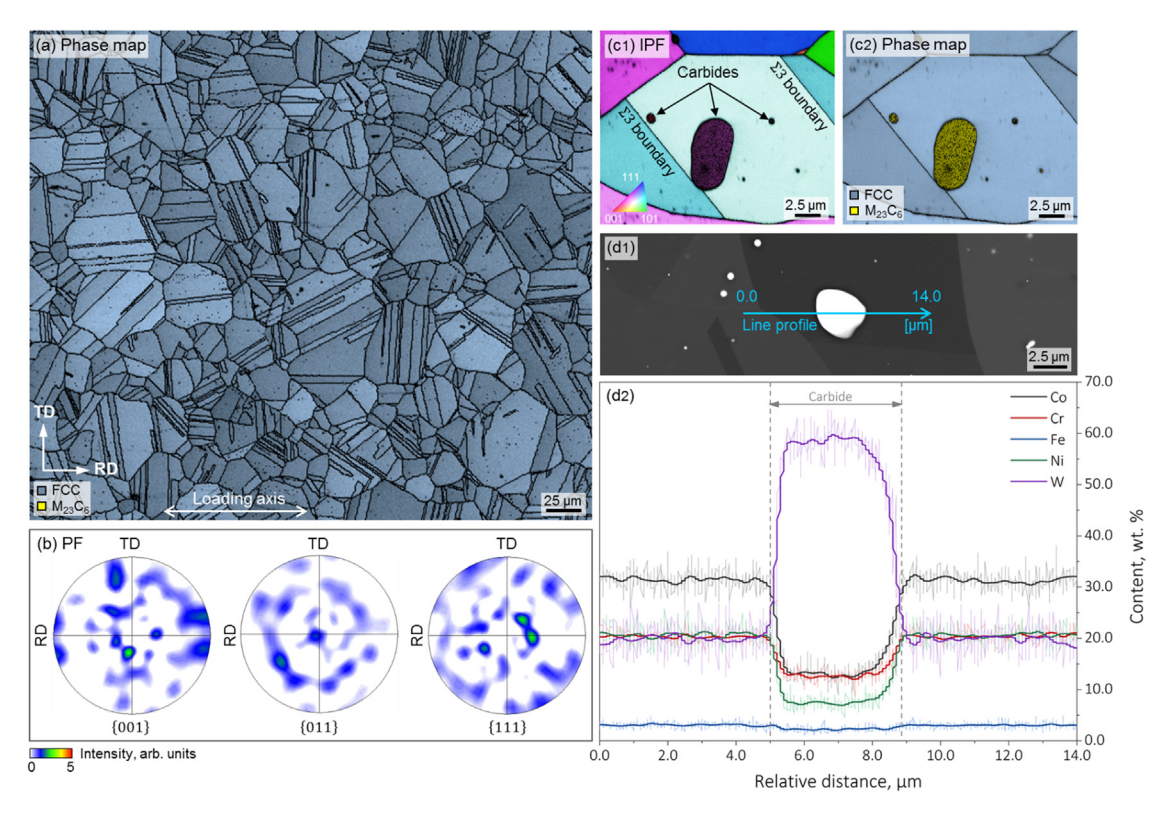
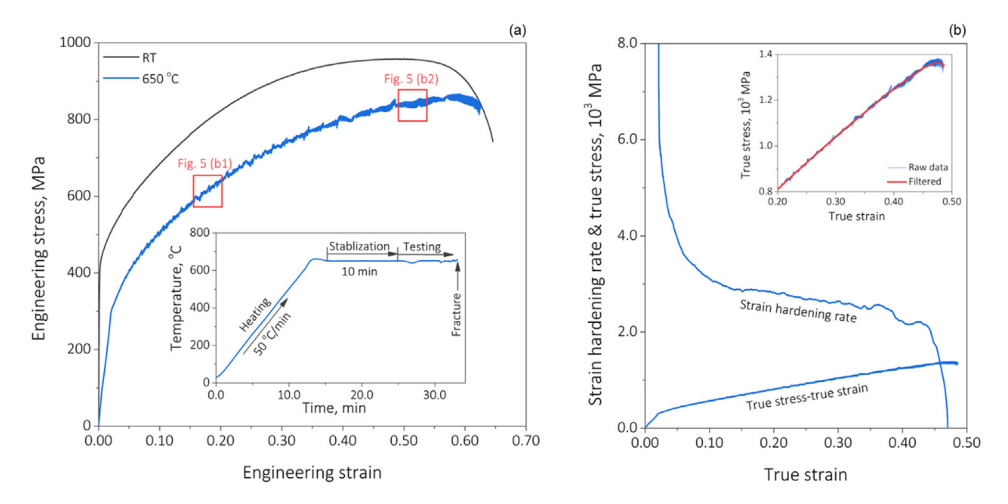


Fig. 2. Microstructure of the CoCrFeNiW-C alloy at the undeformed state: (a) lower-magnification phase map showing the grain morphology; (b) {001}, {011}, and {111} pole figures; (c1) higher-magnification loading direction (LD) inverse pole figure showing the carbide phase; (c2) the corresponding phase map; (d1) and (d2) EDS analysis of the carbide composition.



**Fig. 3.** Uniaxial tensile responses at ambient at elevated temperatures: (a) engineering stress-strain curves.; (b) strain hardening rate curve for high-temperature tensile response. Inset of (a) shows the temperature evolution during testing. Because of the absence of extensometer during the high-temperature measurement, the elastic portion of the blue curve in (a) may not be fully accurate. For the same reason, the elongation results can not be utilized to evaluate the loading-bearing performance of this alloy. Inset of (b) reveals the fast Fourier filtered true stress-strain curve. Abbreviation in the figure: room temperature (RT).

of  $\sim$ 958.1 MPa and a fracture elongation of 0.64. The measured stress-strain curve appears rather smooth, in which no evident serration or noise-like features are observed. However, the uniaxial tensile response demonstrates more complexities at an elevated temperature of 650 °C (inset of Fig. 3(a) which confirms the temperature stability during the test). First, an apparent softening phenomenon occurs, leading to decreased yield strength ( $\sim$ 294.6 MPa, 31.0% decrease) and ultimate tensile strength ( $\sim$ 867.1 MPa, 9.5 % decrease), although maintaining a fracture elongation of 0.62. More intriguingly, the 650 °C stress-strain response exhibits serrated features in two representative enlarged portions of the stress-strain

curves at different plastic strain levels (Fig. 5(b1) and (b2)). Detailed analyses of the serration properties, their latent dynamic features, and microstructural relevance of the serration mode are provided in the latter part of this section and Section 4.1. Here, we firstly employed a fast Fourier filtering algorithm (inset of Fig. 3(b)) to determine the nominal strain-hardening response at 650 °C. Aside from some small irregularities at a true strain level of  $\sim\!0.35$ , which later proved to be related with the onset of Type B serration with much higher stress-drop magnitude (Fig. 5(b2) and Section 4.1), the alloy exhibits a typical monotonically decreasing strain hardening rate.

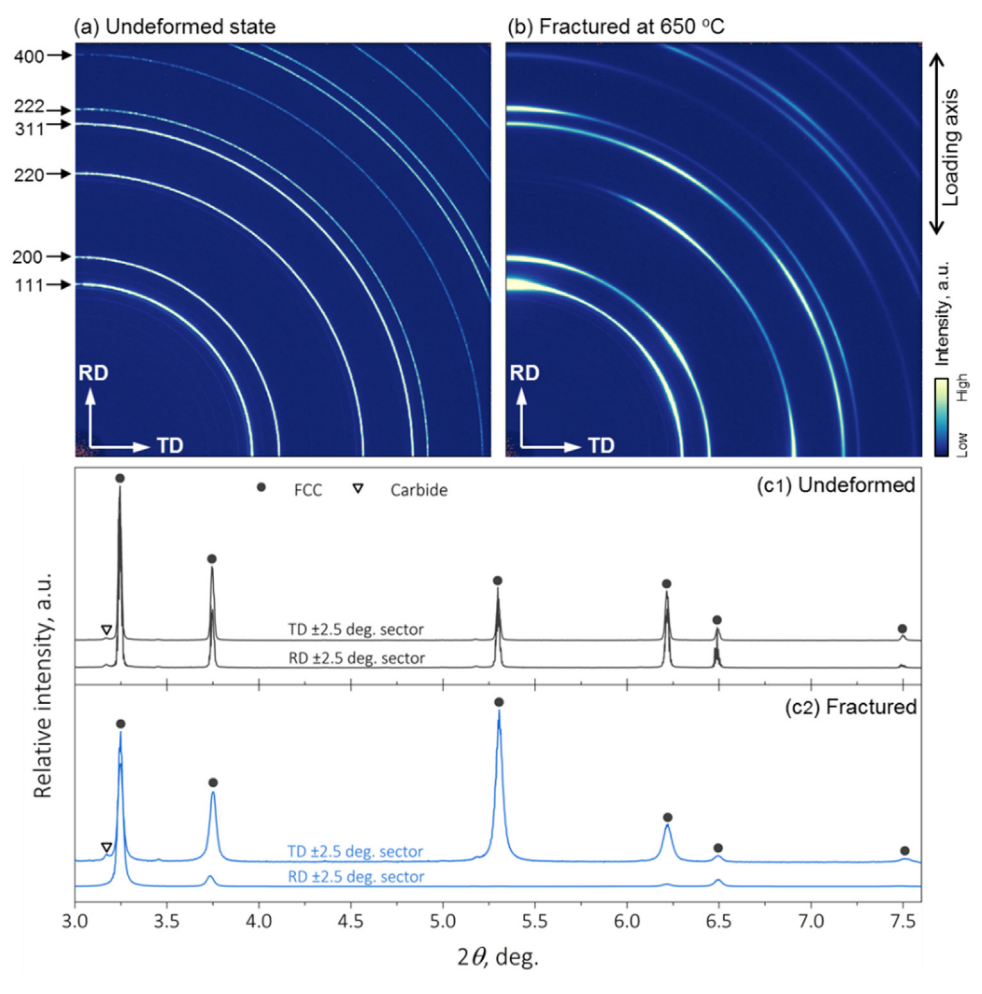


Fig. 4. Phase constitution before and after testing: (a) and (b) two-dimensional SXRD patterns acquired at the undeformed state and after high-temperature testing; (c1) and (c2) integrated one-dimensional diffraction profiles.

As has been reviewed in the literature [16], serrated plastic flow or similar small avalanche incidents during plastic deformation can either be mediated by dislocation plasticity or by displacive phase transformations. To rule out this ambiguity in the discussion onwards, SXRD patterns of the CoCrFeNiW-C alloy were acquired at the undeformed state and after 650 °C tensile test. The two-dimensional diffractograms and the azimuthally integrated profiles (5° sectors along loading and transverse directions) are shown in Fig. 4. Comparison between Fig 4.(c1) and (c2) indicates that the major phase constitution of this alloy maintains unchanged after testing at high temperature, namely, the matrix FCC phase along with the M23C6 carbide phase. It is recognized that although the apparent lattice constant of the matrix FCC phase exhibits a  $\sim 0.31\%$  expansion along the loading direction ( $a^{LD}=3.594$   $\overset{\circ}{A}$  ) and a  $\sim 0.42\%$  contraction along the transverse direction ( $a^{TD} = 3.584 \text{ Å}$ ) due to the Poisson's effect, the widely documented plastic strain-induced hexagonal phase in Co-based alloys [14] is absent in the present alloy. The stability of the FCC phase at the deformation temperature narrows down the discussion of the serration mechanisms to dislocation plasticity. EDS analysis also confirms that no evident compositional change took place in the M<sub>23</sub>C<sub>6</sub> phase (Supplementary Fig. S3). It should be noted that the two-dimensional diffractograms (Fig. 4(b)) highlight the diminished intensity of 220 reflection group along the loading direction after testing. This feature, as revealed in the literature [14], is largely ascribed to the characteristic deformation texture in FCC metals. Such crystallographic information also indicates the absence of dynamic recrystallization in the present experiment.

Given the dislocation-dominated plastic flow response, the commonly observed serration modes can be potentially categorized into four groups on the basis of their phenomenological features [16]:

- Type A serration (Fig. 5(a1)): sporadic stress-drop phenomenon while majority of the stress-strain (or stress-time) curve remains smooth.
- Type B serration (Fig. 5(a2)): high frequency and small fluctuations approximately at (or above) the general flow stress level.
- Type C serration (Fig. 5(a3)): large magnitude stress drop incidents that take place below the general flow stress level (note this difference between Type B and Type C serrations).
- Type D serration (Fig. 5(a4)): plateau-like features in the stressstrain response (i.e. strain bursts), mostly occur in displacement controlled measurements.

As seen in the magnified true stress-true strain plots, depending on the plastic strain level, the present alloy exhibits the following serration features: (1) mixed Type A and B serrations at a moderate deformation level ( $\varepsilon_{true} < 0.25$ ). In this regime, a few intermittent large stress drops (see red arrows in Fig. 5(b1) as a guide) accompanied by continuous small stress fluctuations occur; (2) dominant Type B serrations at an intermediate deformation level ( $0.25 < \varepsilon_{true} < 0.35$ ); and (3) Type B serrations with much higher magnitudes at a higher deformation level ( $\varepsilon_{true} > 0.35$ , Fig. 5(b2)).

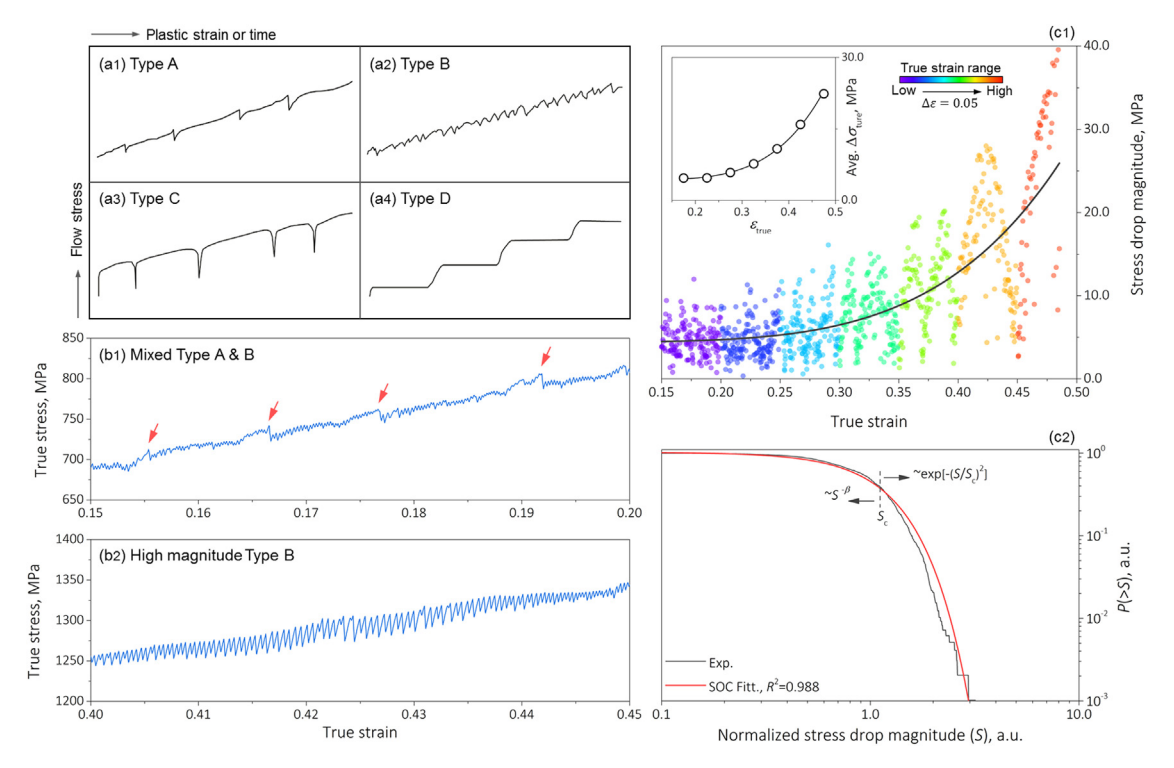


Fig. 5. Characteristics of serrated plastic flow: (a1)-(a4) schematics of four common types of serration modes; (b1) and (b2) operative serration modes at moderate and high deformation levels; (c1) statistical distribution of the stress drop magnitude as a function of increasing applied true strain (color scale here is a guide to the eye to reflect the deformation level); (c2) regression analysis using a self-organized critical dynamic formalism. Abbreviations in the figure: averaged (avg.), self-organized criticality (SOC).

Clearly, these varying phenomenological features and the evolving stress drop magnitude signify the complex interactive mechanisms between mobile dislocations and microstructural constituents. To quantify this, and in light of the scale-free nature of dislocation motion [38], we start with a statistical approach, aiming to clarify the regularity of the serration incidents firstly in the stress series. The stress drop magnitude ( $\Delta \sigma$ ) in each serration is measured for all 992 incidents throughout the whole plastic regime; they are categorized by a 0.05 true plastic strain incrementation and plotted in Fig. 5(c1). Here the use of color scale is given as a guide to the eye to qualitatively reflect the increase in deformation level. In the entire analyses, stress fluctuations smaller than 0.5 MPa are considered as random noise during the test. The inset of Fig. 5(c1) shows that the arithmetically averaged stress drop in each 0.05 true plastic strain group reveals a monotonically increasing tendency as the global plastic strain elevates. Before statistical assessment, however, a normalization of these datum points is needed, because the contribution from strain hardening (Fig. 3(a) and (b)) causes a systematic shift to the statistics.

Through a power function regression analysis of Fig. 5(c1), i.e.  $\Delta \sigma = \psi(\varepsilon)$ , the solid black line, the dimensionless stress drop magnitude dataset,  $S = \Delta \sigma/\psi(\varepsilon)$ , is then taken into consideration (Supplementary Fig. S4). Resorting back to the scale-free concepts of general avalanche incidents, Bak et al. [39,40] firstly introduced a self-organized criticality (SOC) framework, which states:

$$P(>S) \sim S^{-\beta} \exp\left[-(S/S_c)^2\right] \tag{1}$$

Eq. (1) is based on the following theoretical foundations: there exists a certain cut-off magnitude  $(S_c)$  in a series of self-similar avalanche events (denoted as S in Eq. (1)), below which, the complementary cumulative probability distribution (P) obeys a power-law scaling  $(S^{-\beta})$ ; above which, the distribution demonstrates an exponential decay  $(\exp[-(S/S_c)^2])$ . To test this universality hypothesis, the normalized stress drop magnitude was subjected to a Levenberg-Marquardt algorithm for regression analysis based on

Eq. (1). The computational and experimental results are comparatively shown in Fig. 5(c2), in which a good agreement is recognized: the Pearson's *R*-squared value is 0.988 for the 992 datum points. As recognized in other phenomena [41–43], this kind of SOC implies that the system can endure perturbations during the high flow stress level in the alloy. When plastic strain is applied, the alloy manages to buffer the flow stress by a group of self-similar dissipation units with interconnected participants. However, the alloy cannot remain completely tolerant to this effect with increasing flow stress. Therefore, the development of SOC increasingly contributes to the plastic strain, as indicated by the early stress-strain response (Fig. 3).

#### 4. Discussion

#### 4.1. Embedded dynamic features amongst the serration incidents

The statistical assessment of the normalized stress series presented in Section 3.2 highlights the SOC dynamic response of the serration magnitude, i.e. regardless of the increasing plastic deformation level, the operative serration incidents exhibit self-similar features. Such characteristics, on the other hand, also lead to further curiosity about the presence of any latent dynamic features: (1) what kind of statistically correlated feature does the serration duration exhibit? (2) Is there any correlation between the serration duration and its magnitude?

In view of the theoretical framework suggested by Bak et al. [39,40], we use the raw stress-time dataset to determine the true stress-drop magnitude  $(\Delta\sigma)$  and the duration of the stress-drop event  $(\Delta t)$ . An exemplary calculation is provided in Fig. 6(a). Here, the probability density  $(D(\Delta\sigma))$  and  $D(\Delta t)$  in Fig. 6(b) and (c)) is computed through a first-order approximation by using the relative frequency  $(D(\Delta\sigma)) = \delta N/N(\Delta\sigma)$  and  $D(\Delta t) = \delta N/N(\Delta t)$ . Unlike a random distribution, the prototypical histogram of  $N(\Delta\sigma)$  suggests that a large fraction of the serrations yield a moderate magnitude,

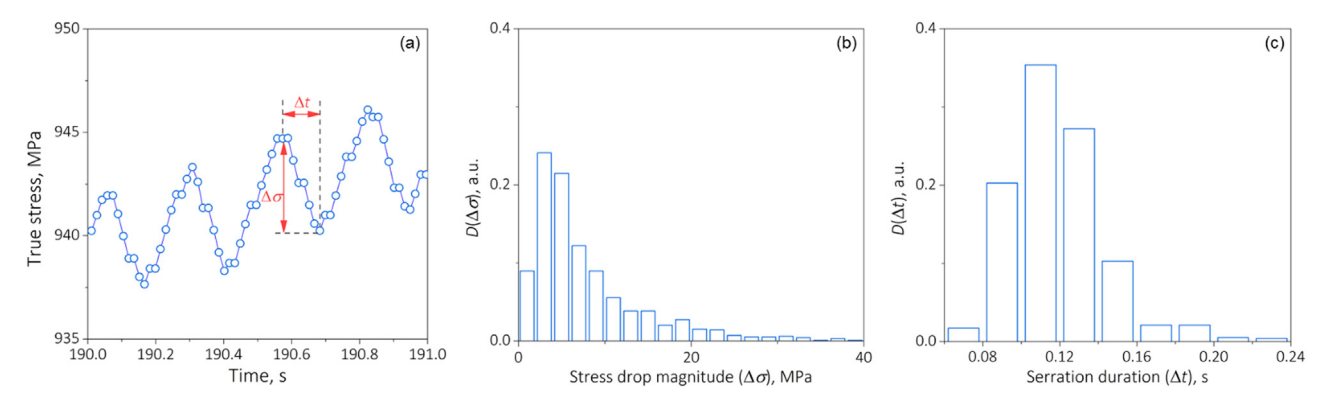


Fig. 6. Statistical assessment of the serration incident on the stress-time series: (a) sketch of the calculation of the stress-drop magnitude and the duration of the stress-drop event; (b) calculated probability density of the serration duration.

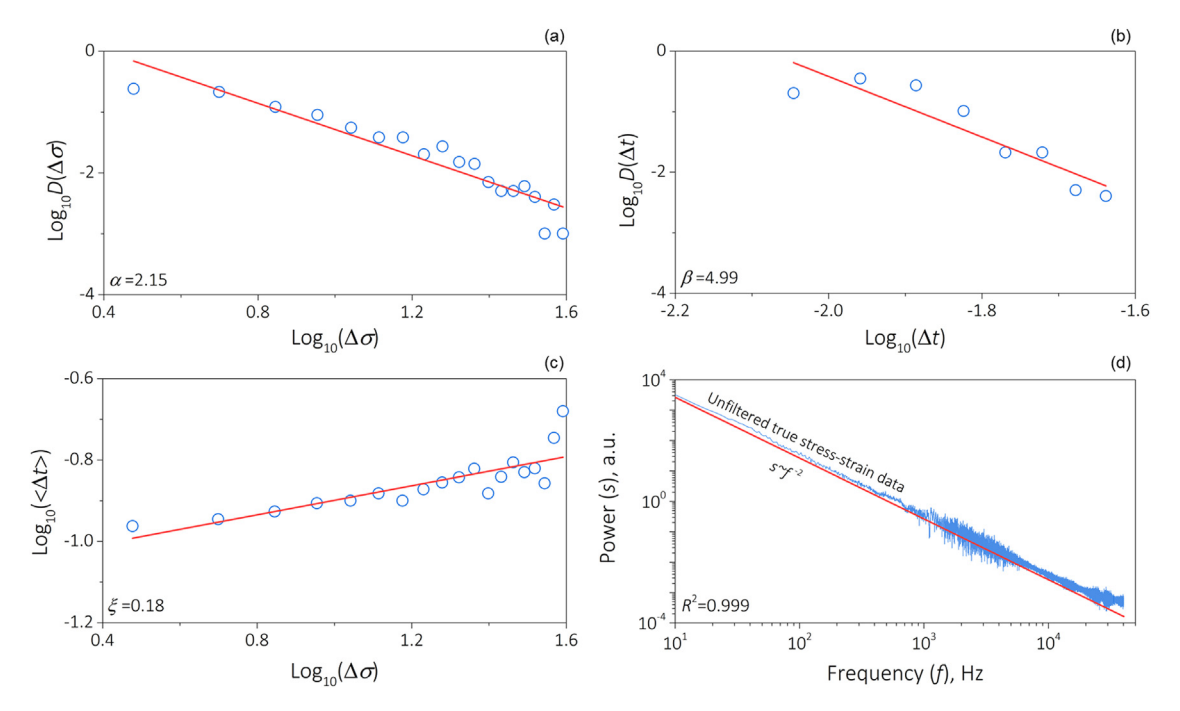


Fig. 7. Embedded dynamic features amongst the serration incidents: (a) power-law scaling in the stress drop magnitude series; (b) power-law scaling in the serration duration series; (c) correlation between mean serration duration and stress drop magnitude; (d) power spectrum of the unfiltered stress-strain data.

followed by an evident decay. Such a feature, when being presented in a Log-Log format (Fig. 7(a)), clearly reveals a power relation:  $D(\Delta\sigma)\sim\Delta\sigma^{-\alpha}$ , where the scaling exponent  $\alpha=2.15$  and crosses  $\sim$ 1.2 orders in  $\Delta\sigma$  (see x-axis of Fig. 7(a)). A similar analysis is also performed for the serration duration, and the results are demonstrated in Fig. 7(b). It is recognized that although a significant power-law scaling  $D(\Delta t)\sim\Delta t^{-\beta}$  also persists (scaling exponent  $\beta=2.15$ ), the serration duration reveals a much less pronounced scaling regime that extends less than  $\sim$ 0.4 order in  $\Delta t$  (see x-axis of Fig. 7(b)).

This kind of distinction in the extent of scaling regime for avalanche magnitude versus its lifetime was firstly documented in the Bak's prototypical sandpile model [39], and was later systematically assessed by numerous large-scale simulations [44,45]. Representatively, in the study of Manna [44] that assessed the spatial-temporal manifestation of SOC dynamics, it was revealed that while the scaling regime for avalanche magnitude can span over  $\sim$ 5 orders, the resulting avalanche lifetime lasted no more than  $\sim$ 3 orders. In recent experimental investigation of model systems [46] and actual material systems [16] that have considered both the magnitude scaling and the duration scaling for avalanche

incidents, the foregoing distinction is also well-confirmed, and the scaling regime for duration barely exceeds  $\sim\!2$  orders. We note that the large scaling exponent  $\beta$  measured in the present alloy requires a high sampling frequency in the time series. In our case, since at least 8 datum points are recorded for the stress drop events identified as serrations (their stress drops are greater than 0.5 MPa), any artifact induced by coarse sampling can be ruled out. A correlation plot for the mean serration duration ( $\langle \Delta t \rangle$ ) versus the magnitude of the stress-drop is shown in *Log-Log* scale in Fig. 7 (c). Likewise, a power relation is observed:  $\langle \Delta t \rangle \sim \Delta \sigma^{-\xi}$ , resulting in a scaling exponent  $\xi=0.18$ . The scaling regime spans over  $\sim\!1.2$  orders for  $\Delta\sigma$  and  $\sim\!0.3$  order for  $\langle \Delta t \rangle$ . The scaling exponent relation [47]  $\alpha=\xi(\beta-1)+1$  is confirmed.

The foregoing analyses have revealed two embedded dynamic features for the present serration incidents: (1) a power-law scaling also exits in the serration duration, although less eminent than the serration magnitude; and (2) a correlation check confirms the power-law scaling between the mean serration duration and the magnitude. The corresponding exponent factors also obey the scaling exponent relation. However, the results shown in Fig. 7(a) and (b) belong to the category of independent non-parametric

statistical study, and the plot in Fig. 7(c) solely confirms a phenomenological correlation. A sanity check is deemed necessary. To avoid redundant mathematics, we employed the power spectrum approach, which concerns the scaling exponents  $\alpha$  and  $\xi$ . Under a quasi-Lorentzian presumption about the energy spectrum for the individual operative event, Kertesz and Kiss [48] derived that if  $2\xi + \alpha > 3$ , the power spectrum follows the scaling relation:  $s(f) \sim f^{-(3-\alpha)/\xi}$ ; on the other hand, if  $2\xi + \alpha < 3$ , then  $s(f) \sim f^{-2}$ , where f is the frequency. In Fig. 7(d) we applied a fast Fourier transform algorithm to compute the power spectrum of the unfiltered true stress-strain data. The entire power spectrum, when being regression assessed by the power relation  $s(f) \sim f^{-2}$ , reveals a near-perfect Pearson's R-squared value of 0.999, following the scaling exponent relation  $2\xi + \alpha < 3$ . This validity examination independently supports our proposed serration magnitude-duration intercorrelated scaling characteristics.

As a final remark, we note that a more dedicated serration magnitude-duration correlation study and thereby the assessment of its stationarity could be carried out by following the generalized Lyapunov's stability concept [49]. This is because the stress signal measured on a time series naturally satisfies the ergodicity presumption when treating the entire serrated plastic flow response as a stochastic process. However, more theoretical effort is required to expand this direction as future work.

#### 4.2. Microstructural relevance of the serration

Earlier analyses showcased in Fig. 5(b1) and (b2) highlight the presence of the following serration modes throughout the entire plastic regime: mixed Type A and B serrations are seen at a moderate plastic strain level and as plastic straining proceeds, higher magnitude Type B serrations start to take place at  $\sim$ 0.35 true plastic strain. Such phenomenological observations also underpin the variation in the governing interaction modes between mobile dislocations and microstructural constituents. Ever since the first theoretical model proposed by Cottrell and Bilby [17], numerous studies have provided direct or indirect evidence for the microstructural origin of the operative serration modes, and the general mechanistic propositions are briefly summarized as follows:

- Type A serration (Fig. 5(a1) and (b1)): locking events due to solute atoms and/or interstitial clouds, whose diffusion kinetics occurs at the same time scale as mobile dislocation's motion upon thermal activation.
- Type B serration (Fig. 5(a2) and (b2)): discontinuous deformation band propagation due to dynamic strain ageing effect of the mobile dislocations within the band.

Given the high carbon concentration in the present alloy (nominally, 0.11 wt%), it can be reasonably deduced that the occurrence of Type A locking serration, although relatively low in its frequency (Fig. 5(b1)), is largely ascribed to potential carbon clouds, which is consistent with the literature [50,51]. However, a quantitative assessment by applying the prototypical pipe diffusion model [52] cannot account for this alloy. This is mostly because the concurrent operation of Type A and B serration invalidates the presumption in these theories that postulate the stationarity of preexisting dislocation junctions. The microstructural origin of the onset of high magnitude Type B serration requires more dedicated effort. We suggest that such a phenomenon can be explained by the interaction between mobile dislocations and L1<sub>2</sub>-type short range ordered domains.

A separate set of single stress relaxation analyses was performed to track the evolution of thermal activation parameters during serrated plastic flow following the methods in Ref. [53]. The major purpose of such measurements is to assess whether the observed serration magnitude increase is correlated with the

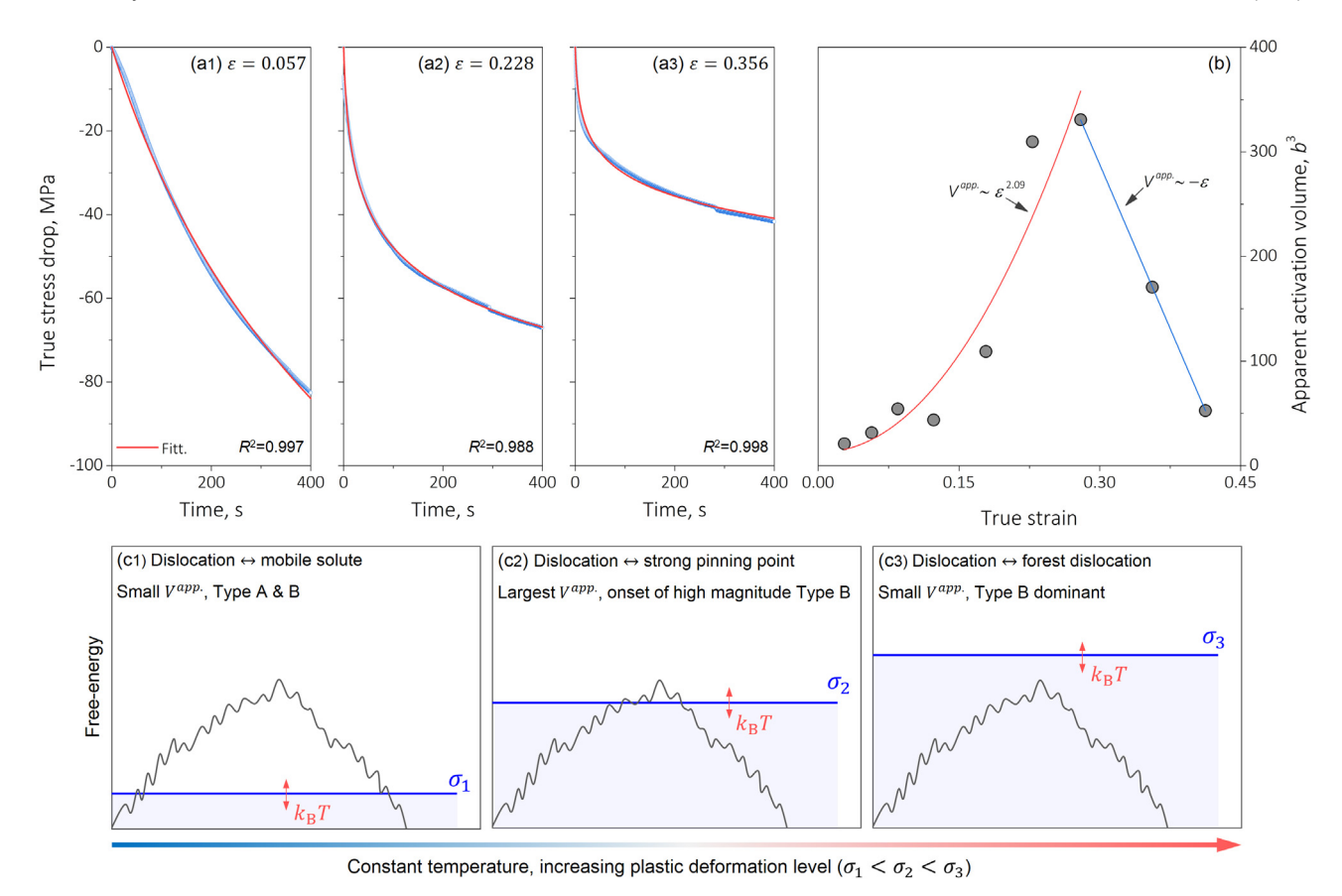
change in the governing thermally-activated process. The theoretical foundations of the stress relaxation test lie in the flow stress-dependent Gibbs free-energy ( $\Delta G(\sigma)$ ) that reflects the energetics of the mobile dislocations to overcome existing obstacles within a microstructure (e.g. interstitial clouds, short range ordered domains, precipitates, and forest dislocations). One of the most important physical quantities that are often involved is the apparent activation volume ( $V^{app.}$ ). By definition, the apparent activation volume quantifies the volume of matter that is associated with a thermally-activated process induced by external loading. In the experimental investigation, the apparent activation volume ( $V^{app.}$ ) is determined by fitting the first relaxation process using a logarithmic attenuation function [53]:

$$\Delta\sigma(t) = -\frac{Mk_{\rm B}T}{V^{app.}}\ln\left(1 + \frac{t}{C_{\rm r}}\right) \tag{2}$$

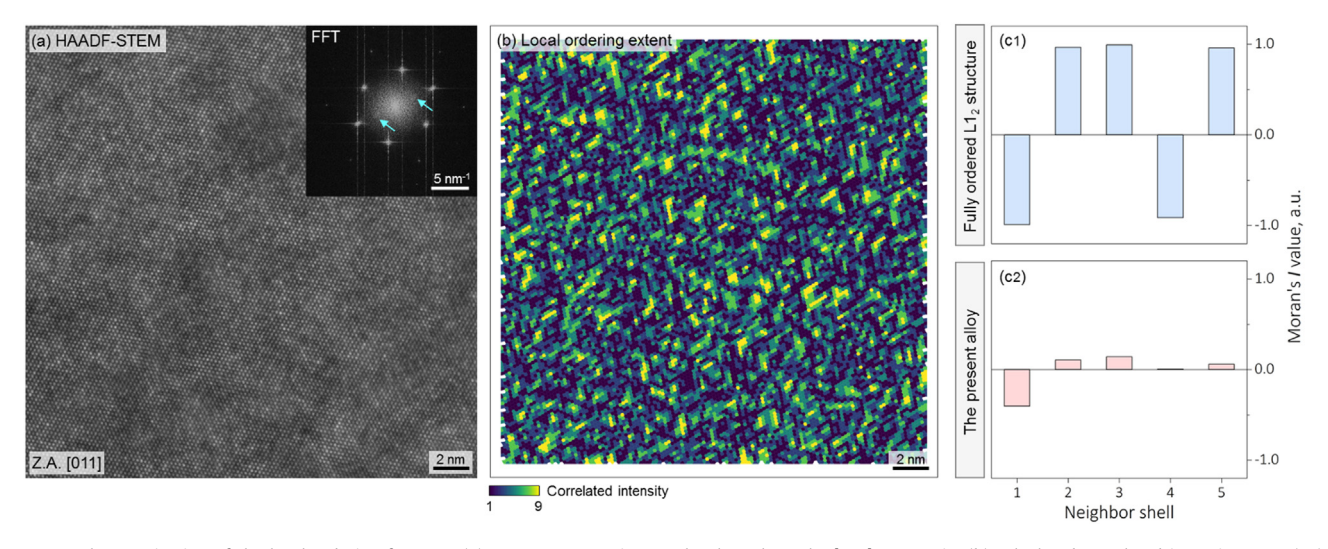
In Eq. (2),  $\Delta\sigma(t)$ ,  $V^{app.}$ ,  $k_{\rm B}$ , T,  $C_{\rm r}$  respectively denote, the true stress drop as a function of time, the apparent activation volume, the Boltzmann constant, the absolute temperature, and the time constant. Some inconsistencies appear in the recent literature [54–57] in exploiting the factor M which converts the normal stress ( $\sigma$ ) to resolved shear stress ( $\tau$ ), i.e. both  $\sqrt{3}$  and 3.06 were applied. The former considers a von Mises criterion for multi-axial yielding, while the latter is the Taylor factor relating together normal stress and resolved shear stress for polycrystalline FCC alloys. Based on the definition of apparent activation volume [55,58],  $V^{app.} = -\partial G(\tau)/\partial \tau|_T = -M[\partial G(\sigma)/\partial \sigma]|_T$ , for a coarse-grained and weakly textured polycrystalline FCC alloy (Fig. 2(b)) subjected to uniaxial tensile loading, M=3.06 is a more appropriate choice.

Fig. 8(a1)-(a3) presents the stress relaxation results (blue unfilled dots) accompanied by the logarithmic regression (red curves) at three representative true stress levels. The blue unfilled dots may not be fully visible in these plots because of the high data acquisition rate employed to track individual serration event (one datum point recorded every 0.015 s). The Pearson's R-squared values all exceed 0.98 given more than 2500 datum points recorded in each relaxation process. The calculated apparent activation volume, after being normalized by  $b^3$  (b the magnitude of the Burgers vector of a perfect dislocation in FCC lattice), reveals an interesting trend: at moderate to intermediate deformation levels,  $V^{app.}$  shows a power-function like increase ( $V^{app.} \sim \varepsilon^{2.09}$ ) as a function of increasing true strain; however, at a true strain level of  $\sim$ 0.30, a clear transition appears, where the  $V^{app.}$  linearly decreases ( $V^{app.} \sim -\varepsilon$ ). In light of the physical meaning of  $V^{app}$ , which quantifies the volume swept by mobile dislocations upon reaching their activated states, the trend captured in Fig. 8(b) combined with the observations in Fig. 5(b1) and (b2) reasonably suggest the mechanistic procedure sketched in Fig. 8(c1)-(c3) using the free-energy landscape concept.

At a moderate deformation level (Fig. 8(c1)), the mobile dislocation tends to interact with the mobile carbon interstitial atoms. With a general applied stress level of  $\sigma_1$ , the contribution from thermal fluctuation  $k_BT$  will enable the dislocation to escape from small local energy traps provided by the mobile carbon solute. Such an operative deformation micro-event will bring about Type A serration along with a small  $V^{app.}$ , as supported by Figs. 8(b) and 5(b1). At a highly deformed state (Fig. 8(c3)), although the applied stress level  $\sigma_3$  is able to overcome all microstructural-based pinning contributions, the absence of dynamic recrystallization in the present alloy (see discussion in Section 3.2) leads to an accumulation of forest dislocations. Consequently, the dislocation mean free path  $l \sim 1/\sqrt{\rho^{disloc.}}$  becomes small. Under this condition, the interaction between mobile and forest dislocations will again reveal a small Vapp., as seen in Fig. 8(b). In this conceived theoretical framework, it can be deduced that at an intermediate deforma-



**Fig. 8.** Mechanistic investigation of the serration mechanisms: (a1)-(a3) exemplary stress relaxation processes at three representative true plastic strain levels; (b) measured apparent activation volume as a function of increasing true plastic strain; (c1)-(c3) phenomenological depiction of the energy landscape for deformation micro-mechanisms based on (b).



**Fig. 9.** STEM characterization of the local ordering features: (a) HAADF-STEM micrograph taken along the [110] zone axis; (b) calculated correlated intensity map; (c1) and (c2) comparison between the fully ordered L1<sub>2</sub> structure and the present alloy using the Moran's I statistical methods reported in Ref. [62]. The normalized intensity map to calculate (b) is provided in Supplementary Fig. S5.

tion level (Fig. 8(c2)), if the applied stress level  $\sigma_2$  is sufficiently high for thermal contribution to bring the mobile dislocation over the strongest microstructural pinning sites, a large  $V^{app.}$  together with a noticeable increase in the stress drop magnitude can be expected. (Figs. 8 (b) and 5(b2)). We note that the assumption of the free-energy landscape depicted here has taken the *a priori* presence of strong local pinning spots, for which the experimental evidence is provided next.

Fig. 9 (a) shows the HAADF-STEM micrograph acquired along the [110] zone axis. In addition to the matrix FCC phase, the Fourier transform of the image (inset of Fig. 9(a)) indicates the presence of diffuse  $L1_2$ -type superlattice reflections [1,59]. To quantify, the atom column normalized intensities (Supplementary Fig. S5) are correlated with a kernel reflecting  $L1_2$ -type ordering using the methods described in Ref. [60]. For a disordered FCC structure, the atom column normalized intensities exhibit low cor-

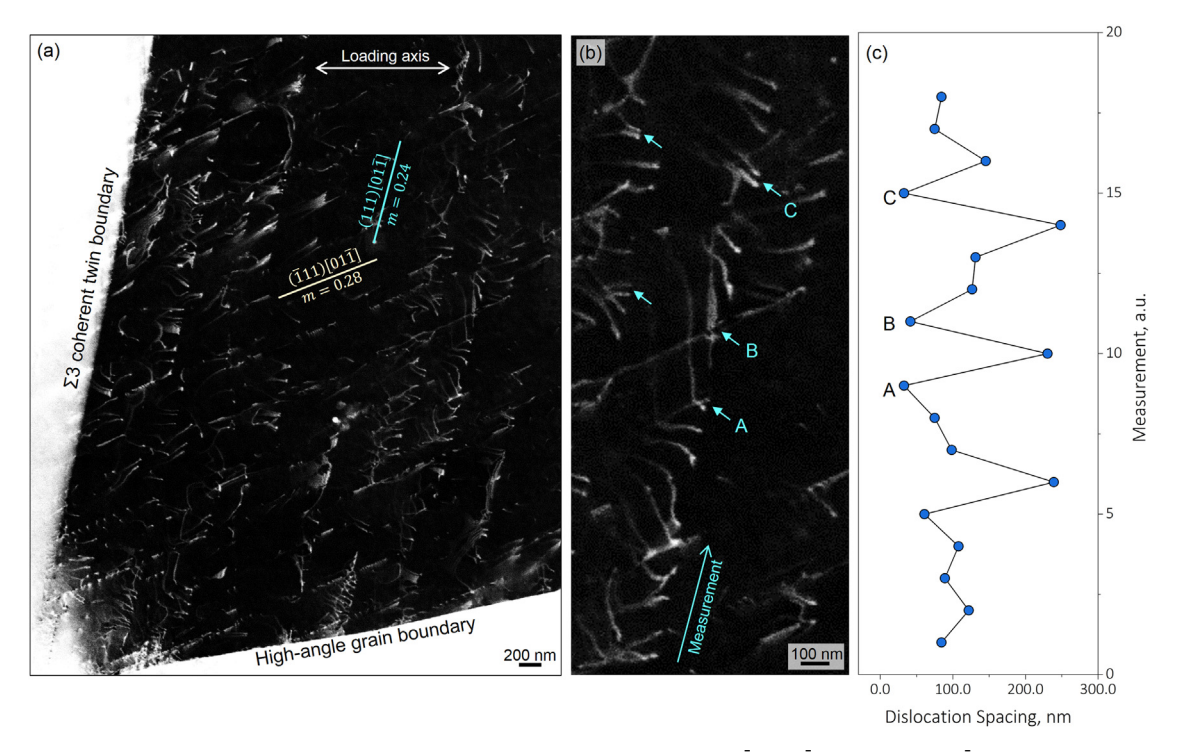


Fig. 10. ECCI characterization of deformation substructures: (a) planar dislocation arrays following the  $(\bar{1}11)[01\bar{1}]$  and the  $(111)[01\bar{1}]$  slip systems with the Schmid factors (m) denoted; (b) higher-magnification ECCI micrograph showing the dislocation pairing feature along one such planar array; (c) measurement of dislocation spacing.

relation with the kernel, while regions showing alternating intensities of L1<sub>2</sub>-type short range order reveal high correlation. As seen in Fig. 9(b), numerous local domains with high correlation to the kernel exist in the present alloy, confirming the presence of L1<sub>2</sub>-type ordering. The length scales and spatial distributions of these domains further indicate their short range ordered (SRO) characteristics. Using the Moran's I statistical methods for analyzing ordering in atomic resolution STEM datasets [61,62], it is also confirmed that the L1<sub>2</sub>-type SRO in the present alloy extends to at least the third nearest neighbor shell in an FCC matrix (Fig. 9(c1) and (c2)).

Zooming out to the meso-scale, the dislocation substructures after 650 °C deformation are next characterized by ECCI. Fig. 10(a) and (b) confirm the strong planarity of perfect dislocation glide, in which organized dislocation arrays are observed following the  $(\bar{1}11)[01\bar{1}]$  and the  $(111)[01\bar{1}]$  slip systems. Measurements of the dislocation spacing along one such array also validate a pairing mechanism (see cyan arrows and Fig. 10(c)). All these observations support the interaction between the L1<sub>2</sub>-type SRO and the mobile dislocations in the following way: the first dislocation destructs the SRO structure due to the applied stress. Because the ordering is only confined to a local region (Fig. 9(b) and (c2)), restoring of such a structure becomes difficult for the following dislocations. The first dislocation therefore encounters the highest slip resistance than all other dislocation gliding along the same pathway. Once the first dislocation overcomes the slip resistance, the accumulated stress is already high enough for all subsequent dislocations to glide [63]. Such a process leads to a plastic deformation which is localized to an individual slip plane where numerous dislocations align up following each other, as seen in Fig. 10(a) and (b).

Because the SRO-modulated slip planarity involves the activation of dislocation sources followed by an abrupt localized deformation much larger than the length scales of diffusive solute atoms, two major consequences are expected: (1) much larger stress drop magnitudes, as observed in Fig. 5(b2); and (2) increased activation volumes at higher plastic stress/strain levels, which is confirmed in Fig. 8(b) and conceived in Fig. 8(c2). It is

worthwhile noting that although the current investigation suggests the diffusive solutes and the  $\rm L1_2$ -type SRO-modulated planar slip are both contributing to the serrated plastic flow at 650 °C, more precise evaluation of the individual contribution still requires future work.

#### 4.3. Temperature effects on serration dynamics

Given the statistical analyses and the mechanistic explorations revealed in the previous sections, a final point that is worthwhile clarifying is the temperature dependence of the serration dynamics. Fig. 11(a1) and (a2) reveal the representative potions of the true stress-strain curves for the present alloy tested at three different temperatures. The same strain rate,  $\dot{\varepsilon}=10^{-3}~{\rm s}^{-1}$  was adopted in these measurements. The entire stress-strain curves are provided in Supplementary Fig. S6. At the intermediate deformation level (0.25 <  $\varepsilon_{true}$  < 0.30) a more pronounced Type C serration occurs as the temperature increases to 750 °C, which is characterized by the more discernable stress drops well below the general flow stress level. Such a trend persists and becomes more noticeable at the higher deformation level (0.35 <  $\varepsilon_{true}$  < 0.40), while the frequency of Type B serration is significantly reduced.

In addition to the phenomenological conclusions of the dominant serration mode change, further analyses were also carried out to assess the latent serration dynamics at the higher temperatures. Following the theoretical framework outlined in Eq. (1), the complementary cumulative probability distributions for the 700 and 750 °C serrations are calculated (Fig. 11(b1) and (b2)). Given the evident increase in the fraction of Type C serration, the SOC characteristics identified earlier (Fig. 5(c2)) are similar. As the testing temperature reaches 750 °C, however, a slight perturbation of the SOC property occurs, which is evident in the reduction in the Pearson's *R*-squared value of 0.965. Moving forward to the spatial-temporal manifestation of the SOC dynamics, we next examine the temperature dependence of the scaling exponents, following Section 4.1. To avoid redundancy in the main text, intermediate



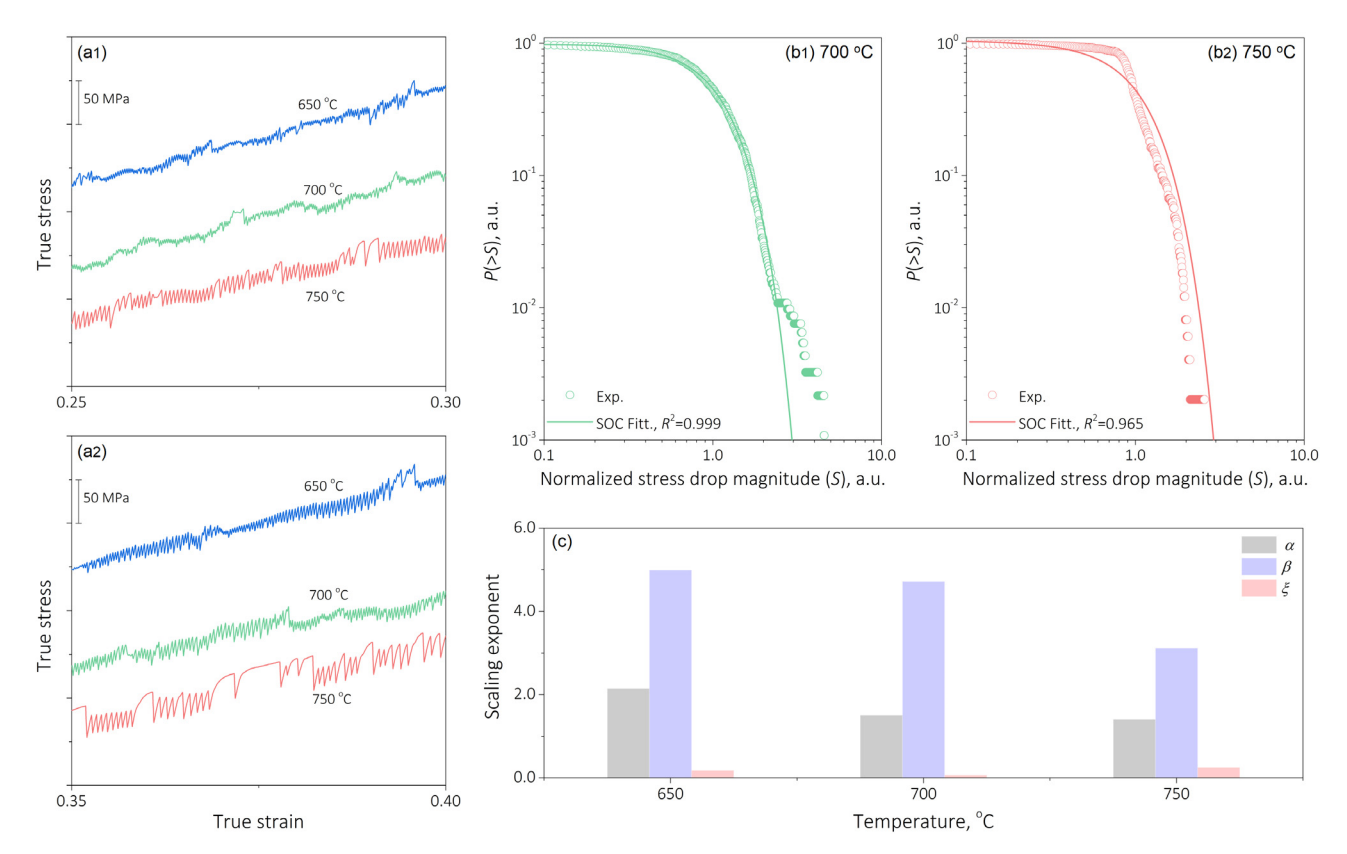


**Fig. 11.** Temperature dependence of the serration dynamics: (a1) and (a2) representative portions of the true stress-true strain curves obtained at 650, 700, and 750 °C under the same strain rate of  $10^{-3}$  s<sup>-1</sup>; (b1) and (b2) complementary cumulative probability distributions of the 700 and 750 °C results analyzed using SOC statistics; (c) box chart for temperature dependence of the scaling exponents.

**Table 1**Temperature dependence of the scaling exponents.

Temperature, °C	α	β	ξ	$2\xi + \alpha$
650	2.15	4.99	0.18	2.51
700	1.51	4.72	0.07	1.65
750	1.41	3.12	0.25	1.91

steps of the analyses are summarized in Supplementary Figs. S7 and S8. The calculation results are summarized in Table 1 with the three critical scaling exponents graphically presented in Fig. 11(c). The scaling exponents  $\alpha$  and  $\beta$  both reveal monotonic decreasing trends as the temperature increases from 650 to 750 °C. Although the exponent  $\xi$  exhibits a non-monotonic evolution trend as a function of temperature, the scaling exponent relation  $\alpha = \xi (\beta - 1) + 1$  is still valid for all three temperatures. Finally, cross-validations were performed using the power spectrum algorithm and the relation  $2\xi + \alpha < 3$  preserves. It is therefore conclusive that in the 650–750 °C temperature range with a  $10^{-3}$  s<sup>-1</sup> strain rate, regardless of the phenomenological changes in serration modes, their latent dynamics consistently follows the SOC.

#### 5. Conclusion

In summary, the present study investigated the plastic deformation response of a CoCrFeNiW-C alloy at an elevated temperature of 650 °C. Using the *in situ* SEM-EBSD technique, statistical analyses, and theoretical calculations, detailed mechanistic studies were executed and the major conclusions are as follows:

- In contrast with a smooth stress-strain response at room temperature, plastic flow of the present alloy at 650 °C exhibits a highly serrated feature, with Type A and B serrations operating at a moderate deformation followed by the onset of a much higher magnitude Type B serration as plastic strain exceeds ~0.30. Scale-free statistics reveal the self-organized critical features amongst the operative serration incidents. Detailed statistical quantifications also verify that the power-law scaling not only exists in the serration magnitude and duration but also presents in the magnitude-duration correlation. These embedded dynamic features are also cross-validated through a power spectrum calculation.
- By combining a time-dependent stress relaxation test and electron microscopy study, it is recognized that the onset of the high magnitude Type B serration at 650 °C can be explained by the interaction between mobile dislocations and L1<sub>2</sub>-type short range ordered domains.
- Temperature dependence of the serration dynamics was further evaluated at 700 and 750 °C using the same  $10^{-3}~\rm s^{-1}$  strain rate. Although Type C serration becomes increasingly predominant, the self-organized critical features of the serration incidents along with the spatial-temporal power-law scaling are maintained regardless of the temperature increase.

#### Data availability statement

The datasets generated during the current study are available from the corresponding author (tasan@mit.edu) upon reasonable request.

#### **Declaration of Competing Interest**

The authors declare that they have no known competing financial interests or personal relationships that could have appeared to influence the work reported in this paper.

#### Acknowledgments

The authors wish to thank the two anonymous reviewers for their significant efforts in providing constructive feedback to this manuscript. S.L.W., D.M., and C.C.T. were financially supported by Allegheny Technologies Incorporated (ATI), Natrona Heights, PA, U.S.A. M.X. and J.M.L. acknowledge support for STEM characterization from the National Science Foundation (No. CMMI–1922206). S.L.W. expresses his gratitude to Drs. Michela Geri, Jinwoo Kim, and Felicity Worsnop for the valuable discussion. Synchrotron X-ray diffraction measurements were carried out at Beamline 11ID-C at the Argonne National Laboratory, Chicago, U.S.A., with the kind support of Drs. Yang Ren and Andrey Yakovenko during the COVID19 pandemic. This work also utilized the MIT.nano Characterization Facilities.

#### Supplementary materials

Supplementary material associated with this article can be found, in the online version, at doi:10.1016/j.actamat.2022.118430.

#### **Appendix**

#### A1. Temperature distribution simulation

To ensure a uniform temperature distribution across the gauge section for the tensile specimen (Supplementary Fig. S1), we have carried out a heat transfer analysis by simulating the steady-state temperature field at 650 °C. The following heat transfer boundary conditions were considered for the present testing setup: (1) ideal thermal conduction between the mechanical clamps and the specimen's end in the vertical direction (considered as a heat sink at 25 °C); (2) thermal radiation at all exposed surfaces with both emissivity and the view factor taken as unities; (3) thermal convection is negligibly small since the test is performed in an SEM's chamber with a vacuum rate greater than  $10^{-2}$  Pa; (4) unexposed surfaces without conduction were modeled as perfectly insulated; and (5) the heating unit in the setup (the flat cylindrical pan in Fig. 1(c)) is considered as a heat reservoir at 650 °C supplied to the sample via perfect thermal conduction. The last condition is considered a good approximation of the reality, as the ceramic heating unit is maintained at temperature by the proportional-integralderivative (PID) controller of an electrical heating input, and as the polished tensile specimen is pressed against the heating pan by tightened springs that maintain contact even through deformation. In total, these boundary conditions reflect a maximized heat transfer condition and therefore show the worst-case temperature homogeneity through the gauge section of the testing sample.

Numerical analysis was carried out in the heat transfer module of a SolidWorks 2020 software using a finite element method. A mesh quality check was conducted using a 4-point Jacobian method, from which a standard mesh with 0.125 mm element size was recognized to provide accurately convergent node temperature values for a reasonable computational expense. The gauge section was formed by  $16 \times 16 \times 72$  tetragonal elements, which enables sufficient node temperature data in our assessment (Fig. 1(d)). Considering the similar physical properties of ferrous elements in the solid state, we have employed the latest thermal physical parameters of Inconel 718 Ni-based superalloys in our simulation. Table A1 lists all the thermo-physical parameters and their quantities utilized in the simulation.

**Table A.1** Thermo-physical parameters utilized in the simulation.

Thermo-physical parameter	Unit	Value	Refs.
Ambient temperature $(T_a)$	°C	25.0	Present work
Heating unit temperature $(T_h)$	°C	650.0	Present work
Alloy emissivity $(\varepsilon_a)$	-	1.0	Present work
Alloy thermal conductivity $(K_a)$	$W \cdot m^{-1} K^{-1}$	254.2	[64]
Alloy specific heat $(C_p)$	$J \cdot kg^{-1}K^{-1}$	0.104	[64]
Alloy mass density $(\rho_a)$	kg⋅m <sup>-3</sup>	$8.11 \times 10^3$	[64]

#### References

- R.C. Reed, The superalloys: Fundamentals and applications, Cambridge University Press. 2006.
- [2] T.M. Pollock, Alloy design for aircraft engines, Nat. Mater. 15 (2016) 809–815, doi:10.1038/nmat4709.
- [3] C. Panwisawas, Y. Gong, Y.T. Tang, R.C. Reed, J. Shinjo, Additive manufacturability of superalloys: process-induced porosity, cooling rate and metal vapour, Addit. Manuf. 47 (2021), doi:10.1016/j.addma.2021.102339.
- [4] J. Koßmann, C.H. Zenk, I. Lopez-Galilea, S. Neumeier, A. Kostka, S. Huth, W. Theisen, M. Göken, R. Drautz, T. Hammerschmidt, Microsegregation and precipitates of an as-cast Co-based superalloy-microstructural characterization and phase stability modelling, J. Mater. Sci. (2015), doi:10.1007/s10853-015-9177-8.
- [5] X. Liu, W. Cai, Z. Chen, Y. Chen, X. Chen, S. Yang, Y. Lu, J. Han, C. Wang, Effects of alloying additions on the microstructure, lattice misfit, and solvus temperature of a novel Co-Ni-based superalloy, Intermetallics 141 (2022), doi:10.1016/j.intermet.2021.107431.
- [6] A. Suzuki, H. Inui, T.M. Pollock, L12-strengthened cobalt-base superalloys, Annu. Rev. Mater. Res. (2015), doi:10.1146/annurev-matsci-070214-021043.
- [7] B. Ohl, D.C. Dunand, Effects of Ni and Cr additions on Γ + Γ' microstructure and mechanical properties of W-Free Co-Al-V-Nb-Ta-based superalloys, SSRN Electron. J. (2022), doi:10.2139/ssrn.4045983.
- [8] S. Neumeier, L.P. Freund, M. Göken, Novel wrought γ/γ' cobalt base superalloys with high strength and improved oxidation resistance, Scr. Mater. 109 (2015) 104–107, doi:10.1016/j.scriptamat.2015.07.030.
- [9] W. Gui, H. Zhang, M. Yang, T. Jin, X. Sun, Q. Zheng, The investigation of carbides evolution in a cobalt-base superalloy at elevated temperature, J. Alloy. Compd. (2017), doi:10.1016/j.jallcom.2016.10.256.
- [10] M. Cartón-Cordero, M. Campos, L.P. Freund, M. Kolb, S. Neumeier, M. Göken, J.M. Torralba, Microstructure and compression strength of Co-based superalloys hardened by  $\gamma'$  and carbide precipitation, Mater. Sci. Eng. A (2018), doi:10.1016/j.msea.2018.08.007.
- [11] K. Yamanaka, M. Mori, S. Sato, A. Chiba, Stacking-fault strengthening of biomedical Co-Cr-Mo alloy via multipass thermomechanical processing, Sci. Rep. (2017), doi:10.1038/s41598-017-10305-1.
- [12] D. Wei, X. Li, S. Schönecker, J. Jiang, W.M. Choi, B.J. Lee, H.S. Kim, A. Chiba, H. Kato, Development of strong and ductile metastable face-centered cubic single-phase high-entropy alloys, Acta Mater. (2019), doi:10.1016/j.actamat. 2019.09.050.
- [13] K. Yamanaka, M. Mori, Y. Koizumi, A. Chiba, Local strain evolution due to athermal  $\gamma \rightarrow \varepsilon$  martensitic transformation in biomedical CoCrMo alloys, J. Mech. Behav. Biomed. Mater. (2014), doi:10.1016/j.jmbbm.2013.12.019.
- [14] S. Wei, C.C. Tasan, Deformation faulting in a metastable CoCrNiW complex concentrated alloy: a case of negative intrinsic stacking fault energy? Acta Mater. 200 (2020), doi:10.1016/j.actamat.2020.09.056.
- [15] A. Suzuki, S.J. Buresh, R. DiDomizio, S.M. Oppenheimer, S. Nag, I.M. Spinelli, P.R. Subramanian, S.G. Pope, J.C. Schaeffer, Ni-Co-based wrought superalloys containing high W-microstructure design for a balance of properties, Miner. Met. Mater. Ser. (2020), doi:10.1007/978-3-030-51834-9\_5.
- [16] Y. Zhang, J.P. Liu, S.Y. Chen, X. Xie, P.K. Liaw, K.A. Dahmen, J.W. Qiao, Y.L. Wang, Serration and noise behaviors in materials, Prog. Mater. Sci. (2017), doi:10. 1016/j.pmatsci.2017.06.004.
- [17] A.H. Cottrell, B.A. Bilby, Dislocation theory of yielding and strain ageing of iron, Proc. Phys. Soc. Sect. A (1949), doi:10.1088/0370-1298/62/1/308.
- [18] Y. Cai, C. Tian, G. Zhang, G. Han, S. Yang, S. Fu, C. Cui, Q. Zhang, Influence of  $\gamma'$  precipitates on the critical strain and localized deformation of serrated flow in Ni-based superalloys, J. Alloy. Compd. (2017), doi:10.1016/j.jallcom.2016.08.194.
- [19] K. Gopinath, A.K. Gogia, S.V. Kamat, R. Balamuralikrishnan, U. Ramamurty, Tensile properties of Ni-based superalloy 720Li: temperature and strain rate effects, Metall. Mater. Trans. A Phys. Metall. Mater. Sci. (2008), doi:10.1007/ s11661-008-9585-3.
- [20] Y.C. Lin, H. Yang, Y. Xin, C.Z. Li, Effects of initial microstructures on serrated flow features and fracture mechanisms of a nickel-based superalloy, Mater. Charact. (2018), doi:10.1016/j.matchar.2018.06.029.
- [21] R. Sharghi-Moshtaghin, S. Asgari, The characteristics of serrated flow in superalloy IN738LC, Mater. Sci. Eng. A (2008), doi:10.1016/j.msea.2007.09.061.
- [22] T. Sakthivel, K. Laha, M. Nandagopal, K.S. Chandravathi, P. Parameswaran, S.P. Selvi, M.D. Mathew, S.K. Mannan, Effect of temperature and strain rate on serrated flow behaviour of Hastelloy X, Mater. Sci. Eng. A (2012), doi:10.1016/ j.msea.2011.12.011.
- [23] L. Laurson, M.J. Alava, 1/f noise and avalanche scaling in plastic deformation,

- Phys. Rev. E Stat. Nonlinear Soft Matter Phys. (2006), doi:10.1103/PhysRevE.74.
- [24] S.M. Keralavarma, W.A. Curtin, Strain hardening in 2D discrete dislocation dynamics simulations: a new "2.5D" algorithm, J. Mech. Phys. Solids (2016), doi:10.1016/j.imps.2016.05.028.
- [25] S. Graff, S. Forest, J.L. Strudel, C. Prioul, P. Pilvin, J.L. Béchade, Finite element simulations of dynamic strain ageing effects at V-notches and crack tips, Scr. Mater. (2005), doi:10.1016/j.scriptamat.2005.02.007.
- [26] A. Marchenko, M. Mazière, S. Forest, J.L. Strudel, Crystal plasticity simulation of strain aging phenomena in  $\alpha$ -titanium at room temperature, Int. J. Plast. (2016). doi:10.1016/j.jiplas.2016.05.007.
- [27] A. Skaugen, L. Angheluta, J. Viñals, Dislocation dynamics and crystal plasticity in the phase-field crystal model, Phys. Rev. B (2018), doi:10.1103/PhysRevB.97. 054113.
- [28] S. Wei, L. Huang, X. Li, Y. Jiao, W. Ren, L. Geng, Network-strengthened Ti-6Al-4V/(TiC+TiB) composites: powder metallurgy processing and enhanced tensile properties at elevated temperatures, Metall. Mater. Trans. A 50 (2019) 3629–3645. doi:10.1007/s11661-019-05244-7.
- [29] W.D. Summers, E. Alabort, P. Kontis, F. Hofmann, R.C. Reed, *In-situ* high-temperature tensile testing of a polycrystalline nickel-based superalloy, Mater. High Temp. (2016), doi:10.1080/09603409.2016.1180857.
- [30] A. Harte, M. Atkinson, M. Preuss, J.Q. da Fonseca, A statistical study of the relationship between plastic strain and lattice misorientation on the surface of a deformed Ni-based superalloy, Acta Mater. (2020), doi:10.1016/j.actamat. 2020.05.029.
- [31] T.R. Bieler, P. Eisenlohr, F. Roters, D. Kumar, D.E. Mason, M.A. Crimp, D. Raabe, The role of heterogeneous deformation on damage nucleation at grain boundaries in single phase metals, Int. J. Plast. (2009), doi:10.1016/j.ijplas.2008.09. 002
- [32] R. Fritz, D. Kiener, Development and application of a heated in-situ SEM microtesting device, Meas. J. Int. Meas. Confed. (2017), doi:10.1016/j.measurement. 2017.07.012
- [33] J. Wang, Y. Zhang, J. Ma, J. Li, Z. Zhang, Microcrack nucleation and propagation investigation of inconel 740H alloy under *in situ* high temperature tensile test, Acta Metall. Sin. (2017), doi:10.11900/0412.1961.2017.00218.
- [34] E. Alabort, D. Barba, S. Sulzer, M. Lißner, N. Petrinic, R.C. Reed, Grain boundary properties of a nickel-based superalloy: Characterisation and modelling, Acta Mater. 151 (2018), doi:10.1016/j.actamat.2018.03.059.
- [35] S. Wei, J. Kim, C.C. Tasan, *In-situ* investigation of plasticity in a Ti-Al-V-Fe  $(\alpha+\beta)$  alloy: slip mechanisms, strain localization, and partitioning, Int. J. Plast. 148 (2022) 103131, doi:10.1016/j.ijplas.2021.103131.
- [36] B.H. Toby, R.B. Von Dreele, GSAS-II: the genesis of a modern open-source all purpose crystallography software package, J. Appl. Crystallogr. (2013), doi:10. 1107/S0021889813003531.
- [37] X. Sang, J.M. LeBeau, Revolving scanning transmission electron microscopy: correcting sample drift distortion without prior knowledge, Ultramicroscopy 138 (2014) 28–35, doi:10.1016/j.ultramic.2013.12.004.
- [38] M. Koslowski, R. LeSar, R. Thomson, Avalanches and scaling in plastic deformation, Phys. Rev. Lett. (2004), doi:10.1103/PhysRevLett.93.125502.
- [39] P. Bak, C. Tang, K. Wiesenfeld, Self-organized criticality, Phys. Rev. A (1988), doi:10.1103/PhysRevA.38.364.
- [40] P. Bak, C. Tang, K. Wiesenfeld, Self-organized criticality: an explanation of the 1/f noise, Phys. Rev. Lett. (1987), doi:10.1103/PhysRevLett.59.381.
- [41] S. Lise, M. Paczuski, Self-organized criticality and universality in a nonconservative earthquake model, Phys. Rev. E Stat. Phys. (2001) Plasmas, Fluids, Relat. Interdiscip. Top., doi:10.1103/PhysRevE.63.036111.
- [42] G. Grinstein, D.H. Lee, S. Sachdev, Conservation laws, anisotropy, and selforganized criticality in noisy nonequilibrium systems, Phys. Rev. Lett. (1990), doi:10.1103/PhysRevLett.64.1927.

- [43] M.N. Najafi, J. Cheraghalizadeh, H.J. Herrmann, Self-organized criticality in cumulus clouds, Phys. Rev. E (2021), doi:10.1103/physreve.103.052106.
- [44] S.S. Manna, Large-scale simulation of avalanche cluster distribution in sand pile model, J. Stat. Phys. (1990), doi:10.1007/BF01015580.
- [45] R. Pastor-Satorras, A. Vespignani, Universality classes in directed sandpile models, J. Phys. A. Math. Gen. (2000), doi:10.1088/0305-4470/33/3/101.
- [46] N. Yoshioka, A sandpile experiment and its implications for self-organized criticality and characteristic earthquake, Earth Planets Sp. (2003), doi:10.1186/BF03351762.
- [47] P. Bak, M. Weissman, How nature works: the science of self-organized criticality, Am. J. Phys. (1997), doi:10.1119/1.18610.
- [48] J. Kertesz, L.B. Kiss, The noise spectrum in the model of self-organised criticality, J. Phys. A. Math. Gen. (1990), doi:10.1088/0305-4470/23/9/006.
- [49] A.M. Lyapunov, The general problem of the stability of motion, Int. J. Control. (1992). doi:10.1080/00207179208934253.
- [50] S.K. Oh, M.E. Kilic, J.B. Seol, J.S. Hong, A. Soon, Y.K. Lee, The mechanism of dynamic strain aging for type A serrations in tensile flow curves of Fe-18Mn-0.55C (wt.%) twinning-induced plasticity steel, Acta Mater. (2020), doi:10.1016/ i.actamat.2020.02.020.
- [51] J.H. Nam, S.K. Oh, M.H. Park, Y.K. Lee, The mechanism of dynamic strain aging for type A serrations in tensile curves of a medium-Mn steel, Acta Mater. (2021), doi:10.1016/j.actamat.2020.116613.
- [52] A.W. Sleeswyk, Slow strain-hardening of ingot iron, Acta Metall. (1958), doi:10. 1016/0001-6160(58)90101-9.
- [53] D. Caillard, J.L. Martin, Thermally activated mechanisms in crystal plasticity, 2003
- [54] Y.M. Wang, A.V. Hamza, E. Ma, Temperature-dependent strain rate sensitivity and activation volume of nanocrystalline Ni, Acta Mater. (2006), doi:10.1016/j. actamat.2006.02.013.
- [55] G. Laplanche, J. Bonneville, C. Varvenne, W.A. Curtin, E.P. George, Thermal activation parameters of plastic flow reveal deformation mechanisms in the CrMnFeCoNi high-entropy alloy, Acta Mater. 143 (2018) 257–264, doi:10.1016/j.actamat.2017.10.014.
- [56] J. Moon, S.I. Hong, J.W. Bae, M.J. Jang, D. Yim, H.S. Kim, On the strain rate-dependent deformation mechanism of CoCrFeMnNi high-entropy alloy at liquid nitrogen temperature, Mater. Res. Lett. (2017), doi:10.1080/21663831.2017. 1323807.
- [57] Z. Wu, Y. Gao, H. Bei, Thermal activation mechanisms and Labusch-type strengthening analysis for a family of high-entropy and equiatomic solidsolution alloys, Acta Mater. (2016), doi:10.1016/j.actamat.2016.08.047.
- [58] A. Argon, Strengthening mechanisms in crystal plasticity, Oxford University Press, 2007, doi:10.1093/acprof:oso/9780198516002.001.0001.
- [59] J. Sato, T. Omori, K. Oikawa, I. Ohnuma, R. Kainuma, K. Ishida, Cobalt-base high-temperature alloys, Science (80-) (2006), doi:10.1126/science.1121738.
- [60] C. Niu, A.J. Zaddach, A.A. Oni, X. Sang, J.W. Hurt, J.M. Lebeau, C.C. Koch, D.L. Irving, Spin-driven ordering of Cr in the equiatomic high entropy alloy NiFeCrCo, Appl. Phys. Lett. (2015), doi:10.1063/1.4918996.
- [61] P.A. Moran, Notes on continuous stochastic phenomena, Biometrika 37 (1950) 17–23, doi:10.1093/biomet/37.1-2.17.
- [62] M. Xu, A. Kumar, J.M. LeBeau, Correlating local chemical and structural order using geographic information systems-based spatial statistics. http://arxiv.org/ abs/2208.11548
- [63] V. Gerold, H.P. Karnthaler, On the origin of planar slip in f.c.c. alloys, Acta Metall. 37 (8) (1989) 2177–2183, doi:10.1016/0001-6160(89)90143-0.
- [64] Special Metals Alloy technical bulletins inconel 718, (2020). https://www.specialmetals.com/documents/technical-bulletins/inconel/inconel-alloy-718.